




Tuning structural, transport, and magnetic properties of epitaxial SrRuO₃ through Ba substitution

Zeeshan Ali ^{1,*}, Zhen Wang,^{1,2,3} Alessandro R. Mazza,^{4,5} Mohammad Saghayezhian,¹ Roshan Nepal ¹,
Thomas Z. Ward,⁴ Yimei Zhu,^{3,†} and Jiandi Zhang ^{1,6,‡}

¹Department of Physics & Astronomy, Louisiana State University, Baton Rouge, Louisiana 70803, USA


²University of Science and Technology of China, Hefei, Anhui 230026, People's Republic of China

³Condensed Matter Physics & Materials Science, Department, Brookhaven National Laboratory, Upton, New York 11973, USA

⁴Materials Science and Technology Division, Oak Ridge National Laboratory, Oak Ridge, Tennessee 37831, USA

⁵Center for Integrated Nanotechnologies, Los Alamos National Laboratory, Los Alamos, New Mexico 87545, USA

⁶Beijing National Laboratory for Condensed Matter Physics, Institute of Physics, Chinese Academy of Sciences, Beijing 100190, People's Republic of China

 (Received 28 November 2022; revised 29 January 2023; accepted 17 March 2023; published 5 April 2023)

The perovskite ruthenates (ARuO₃, A = Ca, Ba, or Sr) exhibit unique properties owing to a subtle interplay of crystal structure and electronic-spin degrees of freedom. Here, we demonstrate an intriguing continuous tuning of crystal symmetry from orthorhombic to tetragonal (no octahedral rotations) phases in epitaxial SrRuO₃ achieved via Ba substitution (Sr_{1-x}Ba_xRuO₃ with 0 ≤ x ≤ 0.7). An initial Ba substitution to SrRuO₃ not only changes the ferromagnetic properties, but also tunes the perpendicular magnetic anisotropy via flattening the Ru–O–Ru bond angle (to 180°), resulting in the maximum Curie temperature and an extinction of RuO₆ rotational distortions at x ≈ 0.20. For x ≤ 0.2, the reduction of RuO₆ octahedral rotational distortion dominantly enhances the ferromagnetism in the system, though competing with the effect of the RuO₆ tetragonal distortion. Further increasing Ba substitution (x > 0.2) gradually enhances the tetragonal-type distortion, resulting in the tuning of Ru-4d orbital occupancy and suppression of ferromagnetism. Our results demonstrate that isovalent substitution of the A-site cations significantly and controllably impacts both electronic and magnetic properties of perovskite oxides.

DOI: [10.1103/PhysRevB.107.144405](https://doi.org/10.1103/PhysRevB.107.144405)

I. INTRODUCTION

Perovskite oxides (ABO₃) show a wide range of emergent functionalities originating from electronic interactions coupled to the octahedral units [1,2]. In a bulk perovskite oxide system, the oxygen octahedral environment is generally controlled via conventional chemical substitution or external stimuli such as hydrostatic pressure or temperature [3–10]. On the other hand, artificial heterostructures can provide a platform with additional structural tuning routes such as epitaxial-strain [11–16], interfacial-octahedral engineering [1,17–20], strain-controlled doping, etc. [21–23]. Heterostructure engineering has been intensively explored in perovskites, due to the strong structure-property coupling which can drive new ground states that are not accessible in bulk [24–28]. In particular, it has been shown that imposing an artificial heterostructure geometry allows effective tuning of octahedral bond angle, which can be used to manipulate spin alignment and magnetization dynamics [17,18,29–34].

Perovskite ruthenates (ARuO₃, A = Ca, Sr, or Ba) are an excellent candidate to explore the connection of magnetic and electronic properties with the local control of structure. In this system, isovalent substitution has been shown to drastically affect the physical properties due to the close

coupling between structural and electron-spin degrees of freedom [35–37]. The replacement of Sr²⁺ (1.44 Å) ions with Ca²⁺ (1.34 Å) ions in bulk family preserves orthorhombic symmetry, yet distinct Ru-O-Ru angles (CaRuO₃ : 148° and SrRuO₃ : 163°) trigger a subtle modification in the Fermi-level density of states, which leads to a nonmagnetic CaRuO₃ (CRO) and ferromagnetic SrRuO₃ (SRO) [35–39]. In contrast, the larger A-site cation Ba²⁺ (1.61 Å) introduces a transition from orthorhombic to cubic symmetry and a suppression of ferromagnetism by changing Curie temperature (T_C) from 160 K in SRO to 60 K in BaRuO₃ [37]. Since the nominal electron counting is not changing, the octahedral angle, as well as A–O and Ru–O bonding nature appear to be the controlling factor, but the dominant driver of this change has still not been identified. How the electronic structure and magnetism evolve with different substitution levels is far from clear. A complicating factor has been the difficulty in synthesizing the Ba-substituted SrRuO₃ single crystals, where high pressures (18 GPa) are necessary to stabilize a perovskite structure [36,37]. This makes engineering perovskite functionalities dependent on finding innovative synthesis routes. In this respect, the application of substrate-induced epitaxial strain delivers an auxiliary approach to high-pressure bulk synthesis and provides a viable platform to stabilize crystalline films with novel phases and multifunctionalities [11,40–44].

In this study, we demonstrate epitaxial stabilization of the Sr_{1-x}Ba_xRuO₃ (0 ≤ x ≤ 0.7) thin films using strain

*zee89ali@gmail.com

†zhu@bnl.gov

‡jiandiz@iphy.ac.cn

engineering. Combining atomically resolved scanning transmission electron microscopy (STEM) imaging, electron energy-loss spectroscopy (EELS), and x-ray diffraction (XRD) along with magnetotransport measurements, we reveal that the lattice structure can be continuously tuned in a series of $\text{Sr}_{1-x}\text{Ba}_x\text{RuO}_3$ ($0 \leq x \leq 0.7$) thin films grown on SrTiO_3 (001). Ba-cation substitution (x) is found to drive the structure from bulklike orthorhombic ($x = 0$) to a tetragonal (no octahedron rotations: $a^0 b^0 c^0$) phase ($x = 0.2$) enabled by change of RuO_6 distortions. Substitution with Ba not only transforms the lattice symmetry but also triggers a modification in Curie temperature and perpendicular magnetic anisotropy (PMA). The resultant tetragonal (without octahedron rotation) structured film at $x \approx 0.2$ is found to be ferromagnetic with the $T_C \approx 145$ K and exhibits the strongest PMA. However, further increasing Ba substitution considerably suppresses the ferromagnetism, especially as $x \geq 0.5$. These results demonstrate that such isovalent A-site substitution has a significant impact on lattice structure which can be used to manipulate electronic and magnetic functionalities.

II. EXPERIMENT METHODS

A. Film targets

The series of $\text{Sr}_{1-x}\text{Ba}_x\text{RuO}_3$ ($x = 0, 0.08, 0.2, 0.5, 0.7$) thin film targets were synthesized by conventional solid-state reaction. The starting materials of SrCO_3 , BaCO_3 , and RuO_2 in stoichiometric ratios were first mixed thoroughly and then heated at 1200°C in the air for 48 h. Regrinding and sintering at 1200°C were performed to increase the chemical homogeneity. The resultant powders were grounded and pressed into pellets (1-inch diameter) under a hydraulic pressure of 1000 psi. The target pellets were then sintered at 1100°C for 48 h in an oxygen atmosphere. To increase the chemical homogeneity and target density, another sintering at 1100°C for 48 h in an oxygen atmosphere was performed.

B. Film growth

The thin films of $\text{Sr}_{1-x}\text{Ba}_x\text{RuO}_3$ were grown by pulsed laser deposition (PLD) at 700°C with an oxygen pressure of 100 mTorr on TiO_2 -terminated SrTiO_3 (001) (STO) substrates. A KrF excimer laser ($\lambda = 248$ nm) with a 10-Hz repetition rate, and with an energy of 300 mJ (laser energy density ~ 1 J cm^{-2}) was focused on $\text{Sr}_{1-x}\text{Ba}_x\text{RuO}_3$ targets. Postdeposition, the films were cooled down at $\sim 10^\circ/\text{min}$ to room temperature in an oxygen atmosphere of 100 mTorr. To monitor the film growth, the *in situ* differentially pumped reflective high-energy electron diffraction was employed. The film thickness was kept at ~ 40 unit cells (u.c.).

C. Scanning transmission electron microscopy and electron energy-loss spectroscopy

STEM and EELS experiments were performed on a 200-kV JEOL ARM electron microscope at Brookhaven National Library equipped with double-aberration correctors, a dual energy-loss spectrometer, and a cold field-emission source. The atomic-resolution STEM images were collected with a 21-mrad convergent angle (30- μm condenser aperture)

and a collection angle of 67–275 mrad for high-angle annular dark-field (HAADF) and 11–23 mrad for annular bright-field (ABF) imaging. The atomic positions were obtained using two-dimensional Gaussian fitting following the maximum intensity. The microscope conditions were optimized for EELS acquisition with a probe size of 0.8 Å, a convergence semi-angle of 20 mrad, and a collection semiangle of 88 mrad. Dual-EELS mode was used to collect low-loss and core-loss spectra simultaneously for energy-drift calibration in the collecting process. EELS mapping was obtained across the whole film with a step size of 0.2 Å and a dwell time of 0.05 s per pixel. EELS background was subtracted using a power-law function, and multiple scattering was removed by a Fourier deconvolution method.

D. X-ray diffraction

Panalytical X'Pert thin-film diffractometer with $\text{Cu K}\alpha$ –1 radiation and a single-crystal monochromator was employed for coupled scans, omega scans, and reciprocal-space mapping of XRD. The half-order integer spot measurements were carried out in a lab-based Malvern Panalytical X'Pert four-circle diffractometer with a collection time of 100–250 s per point.

E. Electron and magnetotransport

The magnetization was measured by using a Quantum Design Superconducting Quantum Interference Device, a reciprocating sample option. The electron transport measurements were performed in a four-probe configuration on a Quantum Design Physical Property measurement system.

III. RESULTS AND DISCUSSION

A. Crystal structure

We have fabricated a series of $\text{Sr}_{1-x}\text{Ba}_x\text{RuO}_3$ ($0 \leq x \leq 0.7$) thin films on SrTiO_3 (001) substrates with a thickness of 40 u.c. Figures 1(a) and 1(b) show the x-ray diffraction (θ - 2θ) coupled scan for $\text{Sr}_{1-x}\text{Ba}_x\text{RuO}_3$ thin films. In Figs. 1(a) and 1(b), the SrTiO_3 (002)_{pc} Bragg's reflection (*) and film peaks (marked with arrows) as well as Laue interferences could be observed, confirming epitaxial stability and good crystallinity of thin films. Here, pc stands for pseudocubic. The XRD of the heteroepitaxial films demonstrates that the perovskite structure can be stabilized using PLD. These results demonstrate the effectiveness of strain-induced epitaxial stabilization of pure-phase perovskite films. This is an important observation as the $\text{Sr}_{1-x}\text{Ba}_x\text{RuO}_3$ perovskite structure in bulk can only be stabilized using high-pressure synthesis [37]. The ambient pressure synthesis favors the development of different polymorphs such as the nine-layered rhombohedral (9R), six-layered hexagonal (6H), and four-layered hexagonal structures (4H) [36,37,45].

The lattice constant extracted from the specular XRD illustrates that the out-of-plane (OP) lattice parameter (c_{pc}) could be systematically modified via Ba substitution in the presence of epitaxial strain [Fig. 1(c)]. For the SrRuO_3 film, the OP lattice parameter is $c_{\text{pc}} = 3.957$ Å, where elongation

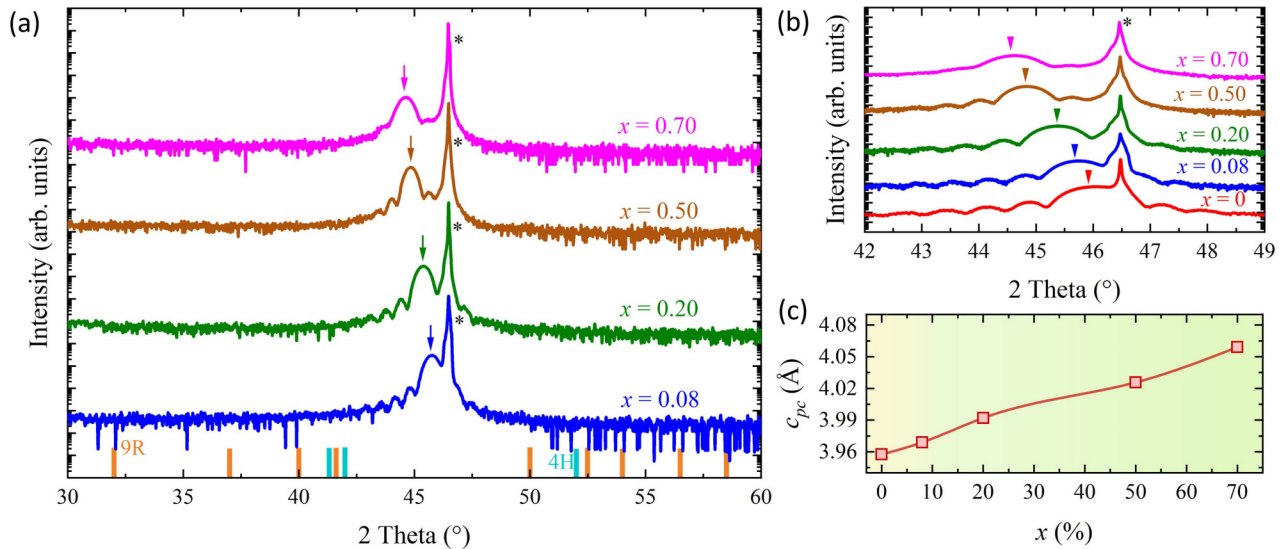


FIG. 1. XRD characterization of $\text{Sr}_{1-x}\text{Ba}_x\text{RuO}_3$ ($0 \leq x \leq 0.7$) thin films at room temperature: (a) Long-range coupled (θ - 2θ) scan, (b) θ - 2θ scan around (002)_{pc} spot, and (c) obtained out-of-plane pseudocubic (c_{pc}) lattice constant vs Ba-concentration (x). SrTiO_3 (002)_{pc} Bragg's reflection and film peaks are marked with * and arrows, respectively.

in the OP direction is caused by compressive strain (bulk $c_{pc, \text{STO}} = 3.905 \text{ \AA} < c_{pc, \text{SRO}} = 3.925 \text{ \AA}$). The systematic Ba substitution of SRO results in (002)_{pc} peak shift to lower 2θ angles [Figs. 1(a) and 1(b)]. The shifting of the peak demonstrates that the OP lattice parameter expands and is summarized as a function of Ba concentration (x) in Fig. 1(c). Such OP lattice enlargement with varying degrees of Ba cation substitution advocates a structural transition.

To further understand the crystal structure of $\text{Sr}_{1-x}\text{Ba}_x\text{RuO}_3$ thin films, we performed reciprocal space mappings (RSM) around (103)_{pc} SrTiO_3 Bragg reflections. The RSM of a SrRuO_3 film is shown in Fig. 2(a). The inspection of film peaks illustrates different Q_z values for (103)_{pc}, (013)_{pc}, (-103)_{pc}, and (0-13)_{pc} diffraction peaks, suggesting an orthorhombic structure. The observation agrees with a GdFeO_3 -type orthorhombic structure [15,46,47]. Furthermore, the film diffraction peaks have identical Q_x with STO as presented in Fig. 2(a), confirming the SRO film is coherently strained. In contrast, for the $\text{Sr}_{0.92}\text{Ba}_{0.08}\text{RuO}_3$ [Fig. 2(b)], the film diffraction peaks have matching Q_z , indicating a tetragonal structural variant. Increasing Ba substitution to 20%

preserves uniform Q_z distribution while maintaining epitaxy to STO but with larger OP expansion [Fig. 2(c)].

B. Atomic-scale structure and composition

We have performed STEM and EELS to reveal microscopically the atomic structure and chemical composition of the films (Fig. 3). The HAADF-STEM (Z-contrast) images show coherent growth of high-quality $\text{Sr}_{0.92}\text{Ba}_{0.08}\text{RuO}_3$ [Figs. 3(a) and 3(b)] and $\text{Sr}_{0.8}\text{Ba}_{0.2}\text{RuO}_3$ [Figs. 3(d) and 3(e)] films on the STO substrate. The large-area HAADF and highly magnified HAADF corroborate dislocation-free structures possessing coherent interfaces and high quality. EELS is also used to extract the elemental profiles of Ba and Sr elements as given in Figs. 3(c) and 3(f). The qualitative elemental profiles were obtained by integrating EELS intensity maps from different regions. The EELS data confirm a homogeneous Ba distribution in the films. The averaged Ba concentration was measured to be 0.07 ± 0.004 in the $\text{Sr}_{0.92}\text{Ba}_{0.08}\text{RuO}_3$ film and 0.20 ± 0.017 in the $\text{Sr}_{0.8}\text{Ba}_{0.2}\text{RuO}_3$ film, which supports the desired Ba concentration of 8% and 20%, respectively.

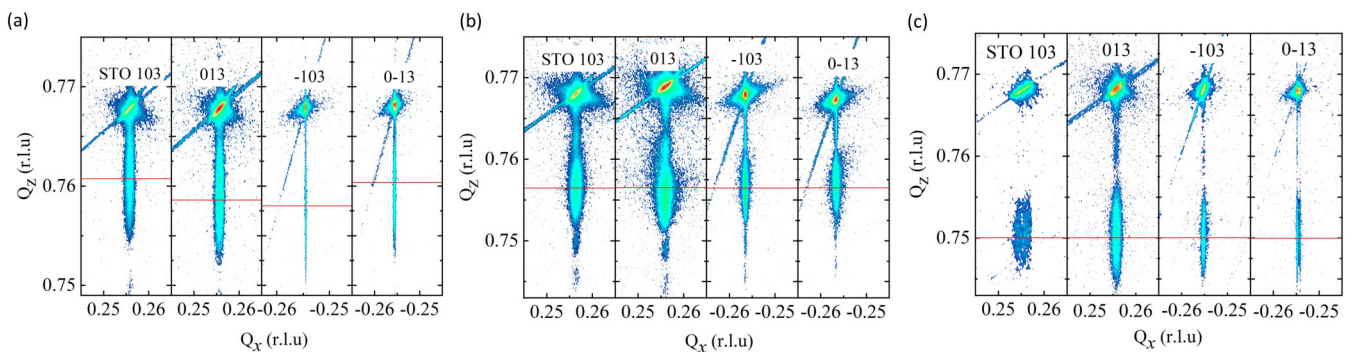


FIG. 2. XRD reciprocal space mapping about the (103)_{pc} reflections from (a) $x = 0$, (b) $x = 0.08$, and (c) $x = 0.2$ of $\text{Sr}_{1-x}\text{Ba}_x\text{RuO}_3$ thin films.

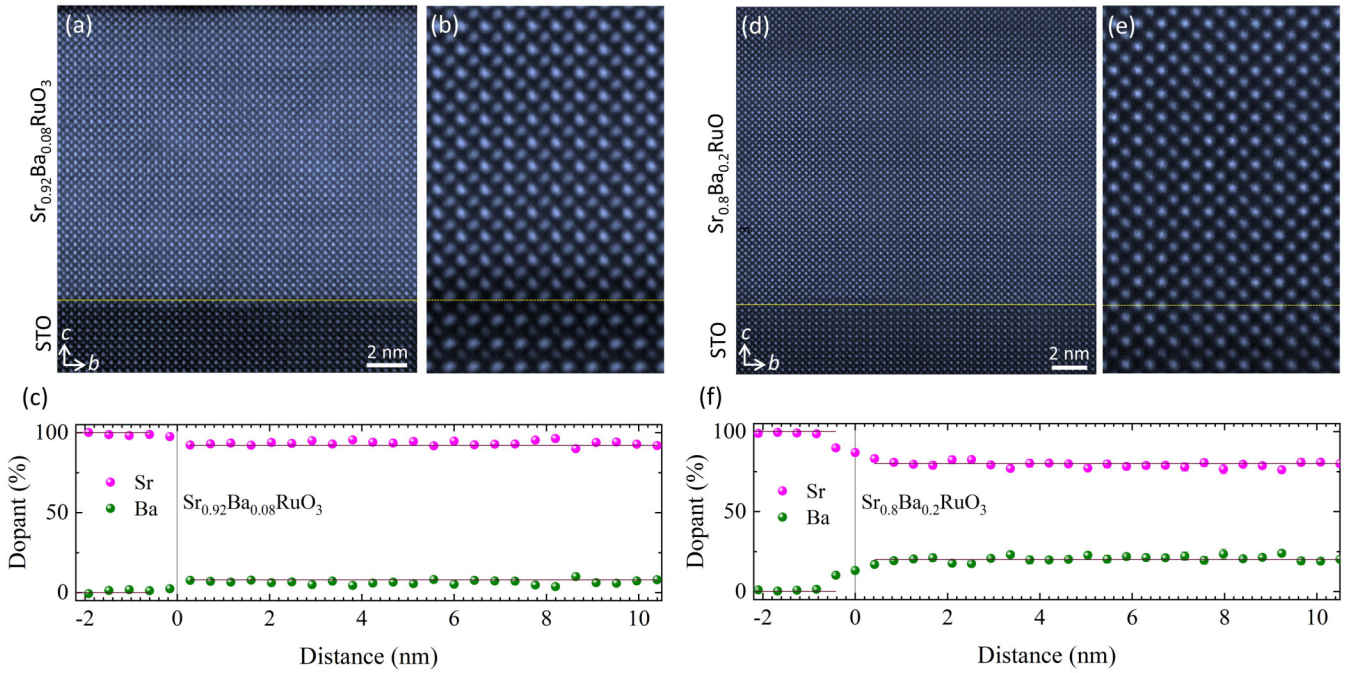


FIG. 3. (a) Large-area HAADF-STEM, and (b) highly magnified HAADF images taken along the $[100]$ -STO direction for $\text{Sr}_{0.92}\text{Ba}_{0.08}\text{RuO}_3$ film. The yellow line marks the substrate-film interface. (c) Dopant-concentration (Sr/Ba) profile of Sr (pink) and Ba (green) extracted from Sr- L and Ba- L edges for $\text{Sr}_{0.92}\text{Ba}_{0.08}\text{RuO}_3$. (d) Large-area, (e) high-magnification HAADF-STEM images taken along the $[100]$ -STO direction, and (f) dopant-concentration (Sr/Ba) profile of Sr (pink) and Ba (green) for $\text{Sr}_{0.8}\text{Ba}_{0.2}\text{RuO}_3$ film.

C. RuO_6 octahedra rotations

To shed light on structural transitions with Ba substitution, we have investigated the RuO_6 octahedra rotations of $\text{Sr}_{1-x}\text{Ba}_x\text{RuO}_3$ thin films using a combination of atomically resolved scanning/transmission electron microscopy (S/TEM) and half-integer x-ray reflections. In ABO_3 perovskites, the Glazer notation is used to describe octahedral rotations [48,49]. In this picture, the BO_6 octahedra rotate about the three orthogonal pseudocubic (pc) crystallographic axes: $[100]_{\text{pc}}$, $[010]_{\text{pc}}$, and $[001]_{\text{pc}}$. The BO_6 rotational magnitudes are specified by letters a , b , and c , referring to the $[100]_{\text{pc}}$, $[010]_{\text{pc}}$, and $[001]_{\text{pc}}$ axes, respectively. The superscripts $+$, $-$, or 0 are used to signify whether the adjacent octahedra around one axis rotates in phase ($+$), out of phase ($-$), or does not rotate (0). In x-ray diffraction, the in-phase rotations ($+$) give rise to $1/2$ - (odd-odd-even) type of reflections, while out of phase ($-$) produce $1/2$ (odd-odd-odd) reflections [47,50–52].

Bulk SrRuO_3 falls into the orthorhombic tilt category $a^+b^-c^-$ ($Pbnm$ space group) as identified by the presence of an in-phase and two out-of-phase rotations [Figs. 4(a) and 4(b)]. Generally, SrRuO_3 films on SrTiO_3 substrates grow in the $[110]_{\text{O}}$ direction, whereas the subscript O stands for orthorhombic notation [14,53], thus providing two possible orthorhombic unit-cell orientations, as given schematically in Fig. 4(c). Consequently, either in-phase $[100]_{\text{pc}}$ or out-of-phase $[010]_{\text{pc}}$ axes align with the $[100]_{\text{S}}$ direction of the STO substrate, leading to two possible domain structures [Fig. 4(c)] referred to as A and B. Here, the subscripts stand for orthorhombic (O), pseudocubic (pc), and substrate (S). In domain A, the in-phase rotation ($+$) axis $[100]_{\text{pc}}$ of the film

lies parallel to the $[100]_{\text{S}}$ of the substrate, i.e., $[100]_{\text{pc}}//[100]_{\text{S}}$ [Fig. 4(c)]. In domain B, the in-phase rotation ($+$) pseudocubic $[100]_{\text{pc}}$ film axis is aligned with the $[010]_{\text{S}}$ STO axis, i.e., $[100]_{\text{pc}}//[010]_{\text{S}}$ [Fig. 4(c)]. The structure in domains A and B are equivalent, but rotated 90° relative to one another [47,53,54]. In our case, the half-angle reflections in Fig. 4(d) establish a single domain (i.e., domain B) structure with an $a^-b^+c^-$ rotation pattern for SrRuO_3 film. In Fig. 4(d), the $(\frac{1}{2}, \frac{1}{2}, \frac{3}{2})$ peak reflects a^- rotation, while the absence of the $(1, \frac{1}{2}, \frac{3}{2})$ excludes the possibility of a^+ . Along the $[010]_{\text{pc}}$ the $(\frac{1}{2}, 1, \frac{3}{2})$ peak suggests b^+ octahedral rotations. Lastly, the occurrence of $(\frac{1}{2}, \frac{3}{2}, \frac{3}{2})$ advocates c^- , and the absence of the $(\frac{1}{2}, \frac{3}{2}, 1)$ rules out c^+ rotation. From these results; the $a^-b^+c^-$ (or equivalently $a^+b^-c^-$ as $a=b$) rotation pattern is valid for SrRuO_3 film, consistent with that of the bulk [21,50]. The preference for domain B-type structures could be attributed to SrTiO_3 substrate vicinality since the modified miscut angle and topography of substrate step edges tends to determine the alignment of the orthorhombic c axis [41,45]. Previous studies have reported that on exactly 001-oriented STO substrate, the volume fraction for A- and B-type domains could be identical, though; depending on the vicinal nature of the (001) SrTiO_3 substrate, one kind of domain formation is preferred [55,56].

In complement to this XRD result, high-resolution STEM images and corresponding fast Fourier transform (FFT) patterns (Fig. 5) of $\text{Sr}_{0.92}\text{Ba}_{0.08}\text{RuO}_3$ film shows that the majority of regions ($\sim 80\%$) are domain B ($[010]_{\text{pc}}//[100]_{\text{S}}$). The coexistence of domain A/B suggests that in-plane rotations are either $-$ or $+$, respectively. Due to the coexisting domain A, and B structure [see Figs. 5(a) and 5(b)], we can acquire

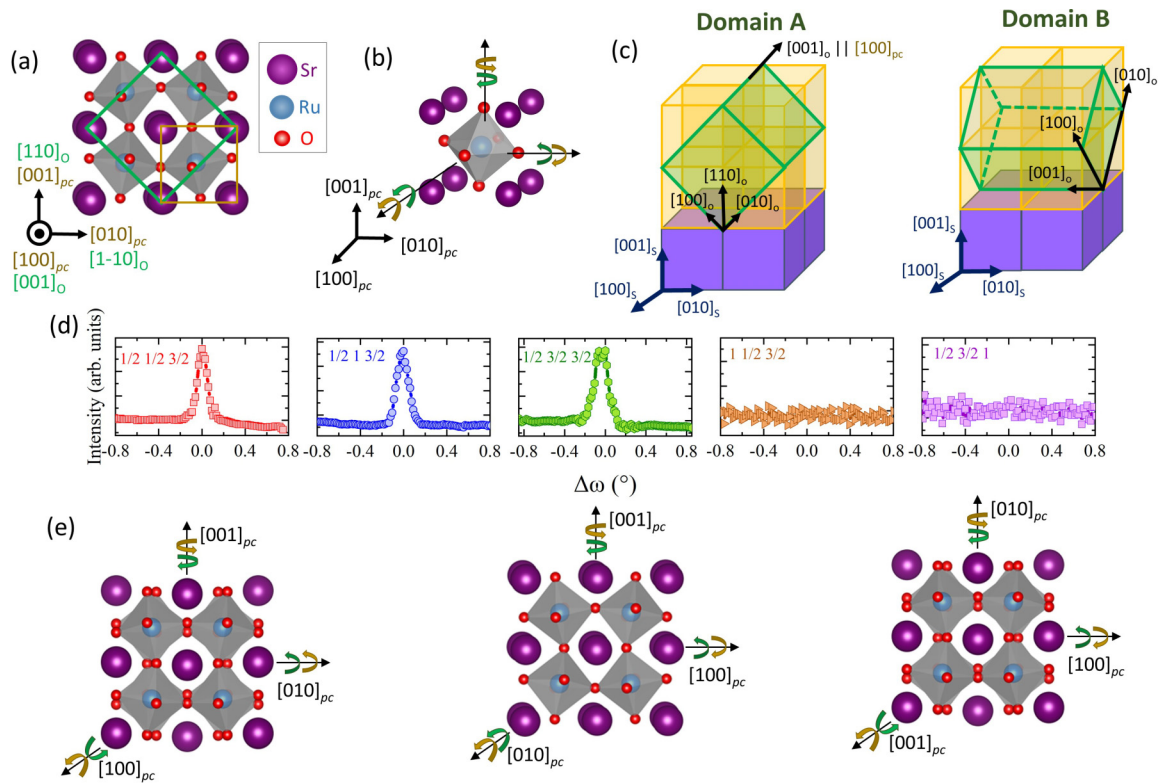


FIG. 4. (a) Crystal structure of bulk SrRuO₃ (SRO). Orthorhombic (O) and pseudocubic (pc) unit cells are indicated by green and orange color, respectively. (b) Pseudocubic unit cell of SRO. Octahedral rotation is in phase along the [100]_{pc} ([001]_O), out of phase about the [010]_{pc} ([1-10]_O), and [001]_{pc} ([110]_O) axes, respectively. (c) Schematic illustrations of orthorhombic SRO unit-cell orientation on a cubic SrTiO₃ substrate with two possible orientations (domains A and B). In-phase rotation (+) axis [100]_{pc} of the film lies within the film plane, which aligns along the [100]_S of the substrate in domain A, and along [010]_S in domain B. (d) Half-integer x-ray reflections for SRO. (e) Representation of octahedral rotation pattern in SRO film. Here, the coordinates are defined with respect to pseudocubic lattice.

simultaneously the projected structures in the [100]_{pc} and [010]_{pc} directions when viewing along the [100]_S direction of the substrate. Figures 5(c) and 5(d) depict high-resolution TEM (HRTEM) images and corresponding FFT patterns, whereas the experimental FFTs are in accordance with the simulated diffraction patterns in the [100]_{pc} [Domain A; see Figs. 5(a) and 5(c)] and [010]_{pc} [domain B; Fig. 5(b) and Fig. 5(d)] directions. The two-domain structures could be distinguished by the presence of characteristic diffraction spots marked as green and red in Figs. 5(c) and 5(d). The structures of domains A and B are identical, but when along the [001]_S direction, as in Figs. 5(a) and 5(b), we can observe simultaneously the RuO₆ tilt in domain A, and A-site cation displacement in domain B [53]. To shed light on octahedra distortion, we have acquired atomically resolved HAADF STEM images of the Sr_{0.92}Ba_{0.08}RuO₃ film [Figs. 5(e) and 5(g)]. The STEM images validate an A-site cation displacement forming a zigzag pattern [Figs. 5(e)–5(g)]. The quantitative analysis of A-site atomic displacements exhibits a value of less than ~0.1 Å versus bulk SrRuO₃ (~0.12 Å), indicative of a suppressed tilt/rotation angle along the in-plane direction [Fig. 5(h)]. Under a compressively strained scenario, we have the following condition: $a_{pc} = b_{pc} < c_{pc}$ (pseudocubic-cell elongation along out of plane); hence, to have considerably smaller a_{pc} and b_{pc} compared to c_{pc} , the octahedron rotation's magnitude along two in-plane axes (a_{pc}

and b_{pc}) would be reduced [47]. Considering the preceding discussion, it is clear that Sr_{0.92}Ba_{0.08}RuO₃ film holds an $a^- b^+ c^-$ (domain B) rotation pattern (only a minor portion is domain A: $a^+ b^- c^-$), but has diminished octahedra rotation magnitude. In other words, epitaxially strained Sr_{0.92}Ba_{0.08}RuO₃ film shows modification of crystal-cell symmetry (tetragonal) and octahedral rotation magnitude but the octahedra rotation pattern ($a^- b^+ c^- / a^+ b^- c^-$) remains intact.

To investigate the crystal structure of Sr_{0.8}Ba_{0.2}RuO₃ film, we have obtained HRTEM images across [100] and [210] STO-substrate directions, as revealed in Figs. 6(a)–6(d). The FFT results [see Figs. 6(a)–6(d)] obtained from HRTEM images confirms the absence of fractional spots, indicating a cubic structure [57]. This is also evident in the annular bright-field STEM image [Fig. 6(e)], where oxygen atoms forming a nontilted octahedron environment could be realized, corroborating an $a^0 b^0 c^0$ perovskite structural symmetry. Furthermore, the half-integer x-ray reflection results revealed in Fig. 6(e) suggest diminishing of characteristic peaks, supporting an $a^0 b^0 c^0$ tilt system. We note that for Sr_{0.8}Ba_{0.2}RuO₃ film, due to compressive epitaxial strain, the out-of-plane lattice expands, while the in-plane lattice parameter is locked with SrTiO₃ (i.e., $a_{pc} = b_{pc} < c_{pc}$); this leads to the pseudocubic-cell elongation along out-of-plane direction (Supplemental Material, Note 1 [58]). Overall, STEM

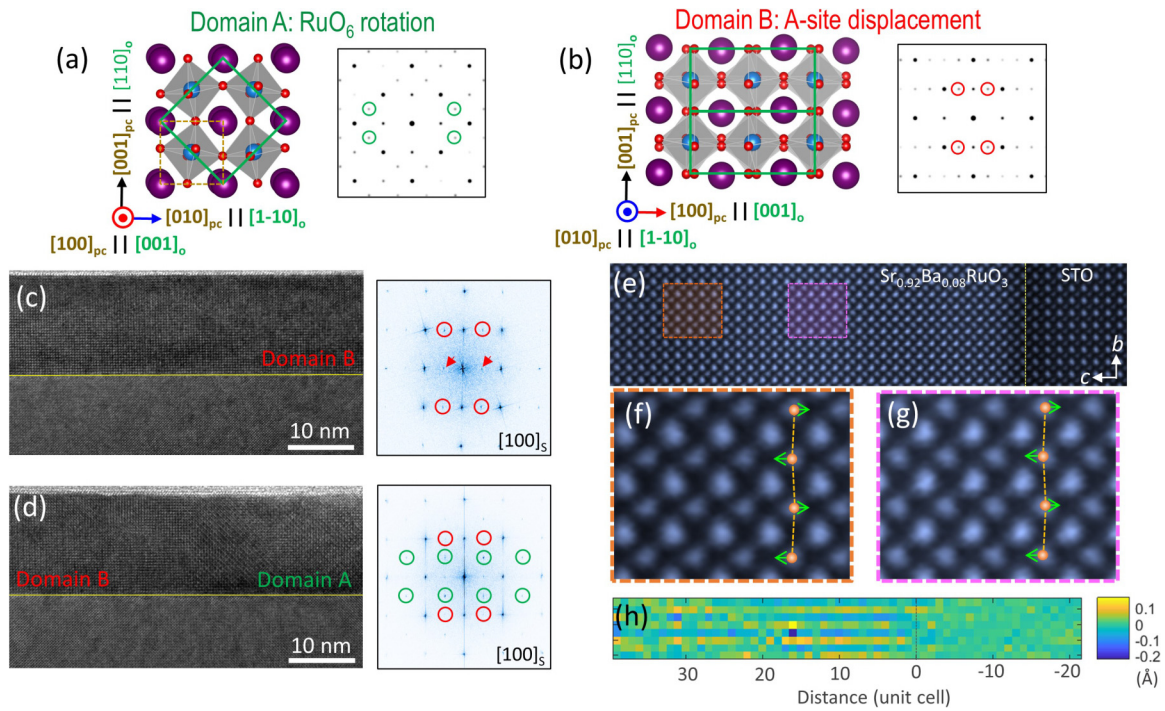


FIG. 5. Domain structure in $\text{Sr}_{0.92}\text{Ba}_{0.08}\text{RuO}_3$ film. (a), (b) Projected crystal structures representing domains A and B along with simulated electron diffraction patterns in the $[100]_{\text{pc}}$ (domain A) and $[010]_{\text{pc}}$ (domain B) directions. (c), (d) High-resolution STEM images with electron beam incident along the $[100]_{\text{s}}$ direction, and corresponding FFT patterns with characteristic fractional spots marked in red (domain B) and green (domain A), respectively. Forbidden spots marked by the arrows, absent in the simulated electron diffractions, were observed due to multiple scattering of the electron and sample. (e) HAADF image of $\text{Sr}_{0.92}\text{Ba}_{0.08}\text{RuO}_3$ film. Dotted yellow line marks the film-substrate interface. (f), (g) Zoom-in images of the regions marked in panel (e) superimposed by the corresponding A-site cation displacement forming zigzag pattern in the Sr/Ba-O plane. (h) A-site cation displacement as a function of distance from substrate.

structural analysis combined with half-integer x-ray measurements advocate that $\text{Sr}_{0.8}\text{Ba}_{0.2}\text{RuO}_3$ film holds an $a^0 b^0 c^0$ tilt-system, a nonrotational octahedra symmetry typically observed in cubic-type perovskites.

D. Magnetometry

In the following, we proceed to investigate the effects of structural transitions on the functional properties

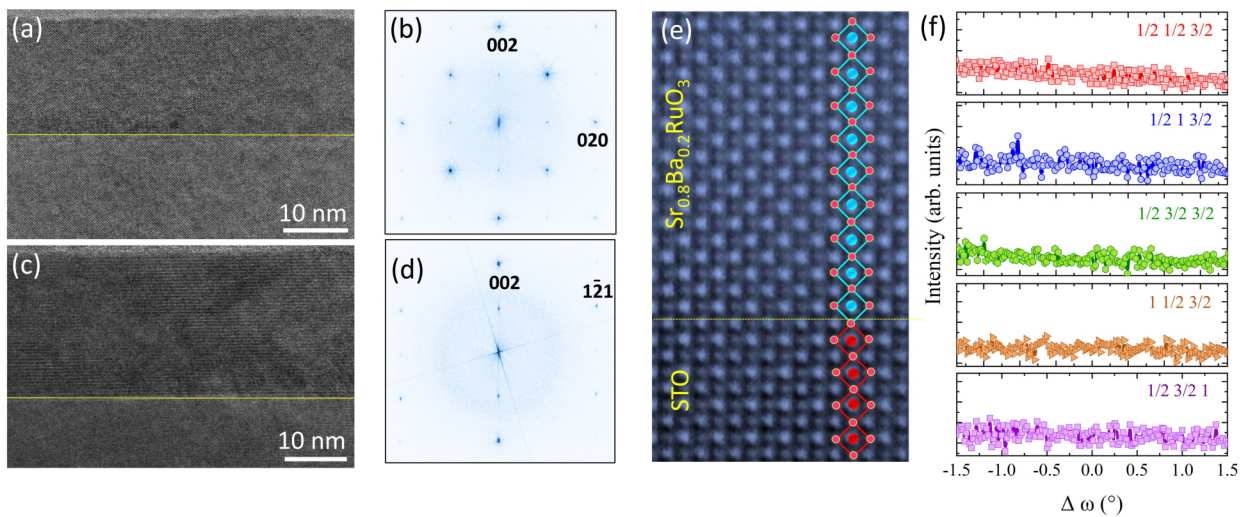


FIG. 6. Crystal structure of $\text{Sr}_{0.8}\text{Ba}_{0.2}\text{RuO}_3$ film determined via S/TEM. (a) HRTEM image taken along the $[100]$ direction, and (b) the corresponding FFT pattern. (c) HRTEM image with (d) FFT pattern taken along the $[210]$ direction. FFT patterns are indexed using the notation of the pseudocubic structure. (e) Highly magnified annular bright-field (ABF) STEM image taken along the $[100]$ direction with projected structural model. Yellow line marks the TiO_2 -(Sr/Ba)O interface. In panel (e) an octahedra without tilt could be observed. (f) Half-integer x-ray reflections for $\text{Sr}_{0.8}\text{Ba}_{0.2}\text{RuO}_3$ film.

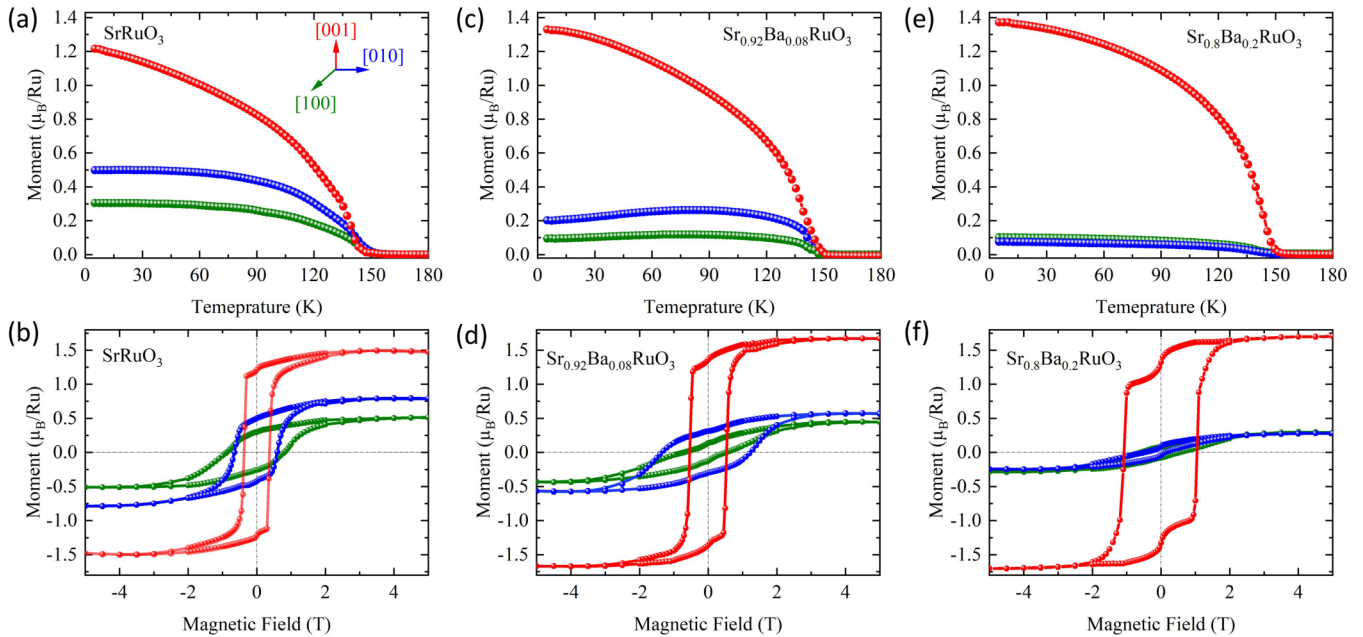


FIG. 7. Magnetization as a function of temperature [$M(T)$], and magnetic field [$M(H)$] for the family of $\text{Sr}_{1-x}\text{Ba}_x\text{RuO}_3$ ($0 \leq x \leq 0.2$) thin films. (a), (b) SrRuO_3 , (c), (d) $\text{Sr}_{0.92}\text{Ba}_{0.08}\text{RuO}_3$, and (e), (f) $\text{Sr}_{0.8}\text{Ba}_{0.2}\text{RuO}_3$.

of $\text{Sr}_{1-x}\text{Ba}_x\text{RuO}_3$ thin films. Figure 7 shows temperature-dependent magnetization [$M(T)$] and magnetic hysteresis [$M(H)$] of $\text{Sr}_{1-x}\text{Ba}_x\text{RuO}_3$ thin films obtained: along the [100] and [010] in-plane directions and along the [001] out-of-plane direction. For $M(T)$, the samples were cooled down in 2000 Oe to 5 K, and in the second step, in presence of 100 Oe, the data are collected during warmup. The orthorhombic SrRuO_3 film undergoes a sharp paramagnetic to ferromagnetic transition in $M(T)$ near ~ 145 K holding a perpendicular magnetic anisotropy (PMA) as in $M(T)$ and $M(H)$, where the easy axis resides in the [001] out-of-plane direction as in Figs. 7(a) and 7(b). We also observed an in-plane magnetic anisotropy, which could be associated with different octahedra rotations along the in-plane directions where rotation is $a^- b^+ c^-$. In contrast, the $\text{Sr}_{0.92}\text{Ba}_{0.08}\text{RuO}_3$ film reveals suppression of magnetic moments across two in-plane directions, while maintaining an out-of-plane easy magnetization axis [Figs. 7(c) and 7(d)]. Interestingly, under structural transition to purely tetragonal (without octahedral rotations: $a^0 b^0 c^0$) form in $\text{Sr}_{0.8}\text{Ba}_{0.2}\text{RuO}_3$ film, the system still exhibits robust ferromagnetism ($T_C \approx 145$ K) with greatly enhanced PMA [Figs. 7(e) and 7(f)]. The configuration of the magnetic spins along two in-plane moments is highly suppressed, which leads to an isotropic in-plane magnetic response in $\text{Sr}_{0.8}\text{Ba}_{0.2}\text{RuO}_3$ film.

E. Electric transport

To investigate the itinerancy of $\text{Sr}_{1-x}\text{Ba}_x\text{RuO}_3$ thin films, the temperature-dependent resistivity [$\rho(T)$] measurement is revealed in Fig. 8(a). All films exhibit a metallic behavior of decreasing resistivity with kinks in resistivity occurring at temperatures coinciding with paramagnetic to ferromagnetic transition temperatures. The kink corresponds to T_C and is clearly visible in the resistivity derivative ($d\rho/dT$) [inset,

Fig. 8(a)], which arises from magnetic scattering and is related to a linear- $\rho(T)$ modification to a $\rho(T)-T^2$ behavior [59,60]. Additionally, we have measured the magnetoresistance: $\text{MR} = [R(H) - R(0)]/R(0)$, where $R(H)$ and $R(0)$ are the resistances with magnetic field and without magnetic field, respectively [Figs. 8(b)–8(d)]. For MR, the external magnetic field was applied along the film normal. We note that in the paramagnetic phase, the MR exhibits a parabolic shape, while a negative, nonparabolic MR appears in FM phase [20,61–67]. In this case, the presence of hysteretic MR at the lowest temperature of 5 K [Figs. 8(b)–8(d)] confirms the existence of robust ferromagnetic ordering in SrRuO_3 , $\text{Sr}_{0.92}\text{Ba}_{0.08}\text{RuO}_3$, and $\text{Sr}_{0.8}\text{Ba}_{0.2}\text{RuO}_3$ thin films. It is noted that the MR magnetic hysteresis endures up to ~ 100 K, whereas above 100 K, a nonparabolic MR persists up to ~ 145 K. These observations approve that the systems under study hold a clear ferromagnetic order up to ~ 145 K.

F. Anomalous Hall

The anomalous Hall effect (AHE) is investigated to further describe the film's intrinsic magnetization behaviors. The total Hall or transverse resistance is specified as $R_{xy} = R_0H + R_A M$. Here, the first term (R_0H) signifies the ordinary Hall component arising from Lorentz force contribution with R_0 being the ordinary Hall coefficient and H the magnetic field. The second term ($\rho_{AHE} = R_A M$) indicates the anomalous contribution, where R_A is the anomalous Hall coefficient, and M the magnetization. For clarification of the anomalous component, we subtracted the ordinary Hall term by linear fitting, which is obtained from the total Hall resistance versus the applied field curve in the high-field regime. The anomalous contribution measured at different temperatures for a series of $\text{Sr}_{1-x}\text{Ba}_x\text{RuO}_3$ ($x = 0, 0.08, \text{ and } 0.2$) thin films is presented in Fig. 9. The reversed hysteretic curve at the lowest

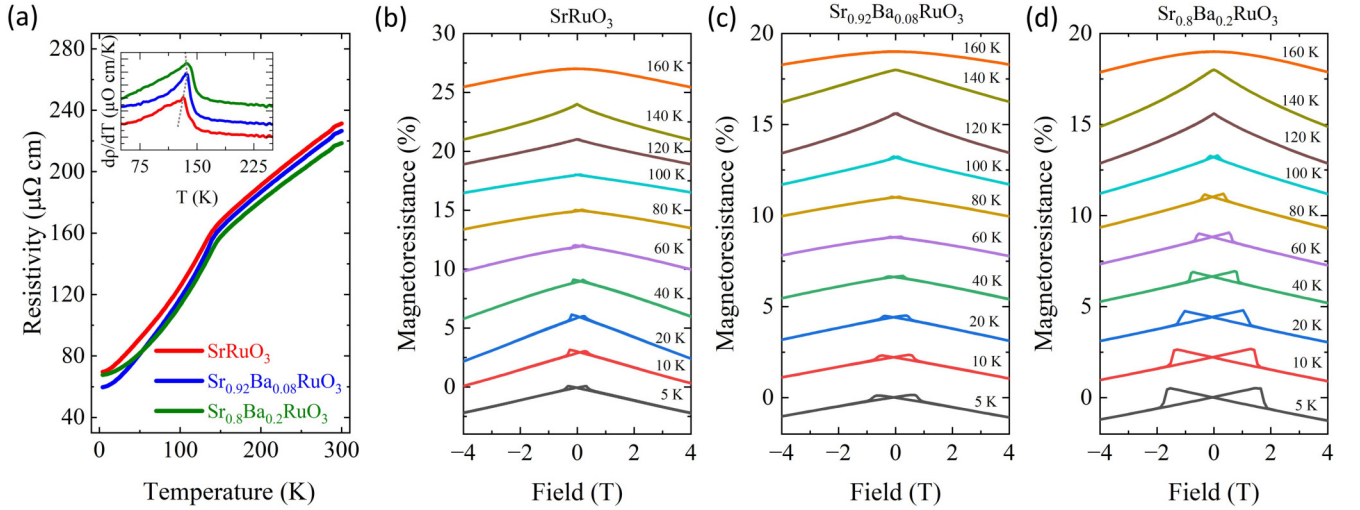


FIG. 8. (a) $\text{Sr}_{1-x}\text{Ba}_x\text{RuO}_3$ ($0 \leq x \leq 0.2$) thin films, temperature-dependent resistivity. Inset in panel (a) is temperature-dependent resistivity derivative ($d\rho/dT$) plotted against temperature (T). Magnetoresistance (MR) of (b) SrRuO_3 , (c) $\text{Sr}_{0.92}\text{Ba}_{0.08}\text{RuO}_3$, and (d) $\text{Sr}_{0.8}\text{Ba}_{0.2}\text{RuO}_3$ thin films measured at different temperatures with magnetic field applied along out-of-plane direction. MR curves are offset to avoid overlap.

temperatures (5 K) signifies strong FM order encompassing a negative R_A [Fig. 9(a)]. The SrRuO_3 ($x = 0$) film displays an inverted magnetic hysteresis loop to 100 K, while at 120 K, a sign reversal is observed [Fig. 9(a)], which indicates R_A sign reversal from negative to positive. Comparable Hall structure with pronounced inverted squarish-shape hysteresis at low temperatures could be interpreted as being the result of strong ferromagnetism in $\text{Sr}_{0.92}\text{Ba}_{0.08}\text{RuO}_3$ [Fig. 9(b)] and $\text{Sr}_{0.8}\text{Ba}_{0.2}\text{RuO}_3$ [Fig. 9(c)] films. Interestingly, the introduction of Ba pushes [Figs. 9(a)–9(c)] the hysteretic flip to higher temperatures (i.e., temperature at which R_A changes sign from positive to negative). Finally, for $\text{Sr}_{0.5}\text{Ba}_{0.5}\text{RuO}_3$ film, the R_A remains negative throughout temperature range [Fig. 9(d)]. The change of Hall sign with increasing Ba concentration is likely associated with two structural effects that can change the Fermi-surface morphology; (1) RuO_6 octahedral rotation reduction, and (2) Ru–O bond-length variation. Tian *et al.* [68] reported that SrRuO_3 with or

without octahedral rotations brings similar behavior of a sign change from negative to positive in Hall conductivity under the changes from compressive to tensile epitaxial strain. On other hand, the larger Ba concentration (especially as $x \geq 0.5$) results in pseudocubic-cell stretching (tetragonal-type distortion: $c_{\text{pc}}/a_{\text{pc}} \gg 1$). This effect leads to further crystal-field splitting (Δ_T) between Ru d orbitals, which in turn changes the Ru orbital energies, and electron occupancy, leading to sign change of anomalous Hall conductivity [13,22,68,69].

G. Ferromagnetism versus Ba substitution

Finally, we discuss the evolution of ferromagnetism and T_C in a series of $\text{Sr}_{1-x}\text{Ba}_x\text{RuO}_3$ as presented in Fig. 10(a). The SrRuO_3 film possesses a T_C of 145 K, while $\text{Sr}_{0.92}\text{Ba}_{0.08}\text{RuO}_3$ film demonstrates a slightly enhanced T_C of 149 K. Remarkably, the $\text{Sr}_{0.8}\text{Ba}_{0.2}\text{RuO}_3$ film with fully suppressed octahedral rotations ($a^0 b^0 c^0$) and flat Ru–O–Ru bond angles has a

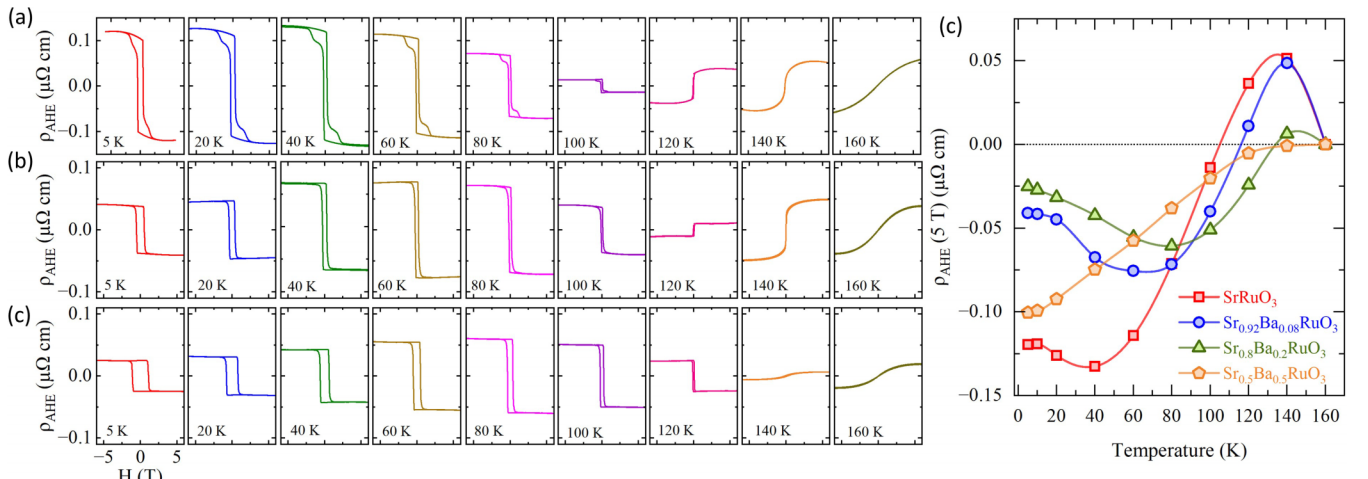


FIG. 9. Anomalous Hall resistivity (ρ_{AHE}) of (a) SrRuO_3 , (b) $\text{Sr}_{0.92}\text{Ba}_{0.08}\text{RuO}_3$, and (c) $\text{Sr}_{0.8}\text{Ba}_{0.2}\text{RuO}_3$. (d) Temperature dependence of anomalous Hall resistivity (ρ_{AHE}) measured at the magnetic-field value of 5 T for series of $\text{Sr}_{1-x}\text{Ba}_x\text{RuO}_3$ ($0 \leq x \leq 0.5$) thin films.

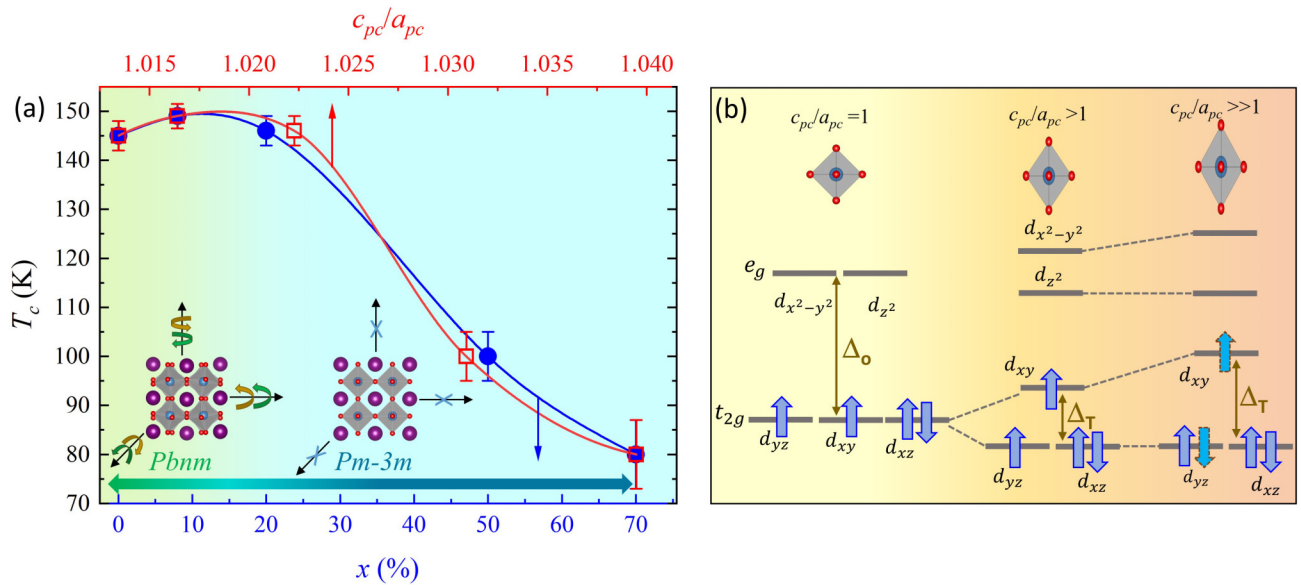


FIG. 10. (a) Phase diagram of T_C in series of $\text{Sr}_{1-x}\text{Ba}_x\text{RuO}_3$ thin films as function of Ba concentration (x), and ratio of out-of-plane (c_{pc}) and in-plane (a_{pc}) pseudocubic lattice constants. (b) Schematic illustration of Ru-4d orbitals. RuO_6 octahedron undergoes tetragonal crystal-field splitting (Δ_T) due to $c_{pc}/a_{pc} > 1$.

nearly identical $T_C \approx 145$ K as compared to the orthorhombic variant. However, the $\text{Sr}_{0.5}\text{Ba}_{0.5}\text{RuO}_3$ film shows lowering of Curie temperature to $T_C \approx 100$ K, which reduced further ($T_C \approx 100$ K) for $\text{Sr}_{0.5}\text{Ba}_{0.5}\text{RuO}_3$ film (Supplemental Material, Note 2 [58]). Moreover, the $\text{Sr}_{0.5}\text{Ba}_{0.5}\text{RuO}_3$ films displays significant suppression of magnetic moment. This suggests, even though the structure remains in a higher-symmetry regime (no octahedron rotations), the larger amount of Ba-cation implantation introduces some subtle changes in electronic and magnetic structure, which condenses the ferromagnetic order. It is worth to note that in the $\text{Sr}_{1-x}\text{Ba}_x\text{RuO}_3$ bulk series, the orthorhombic-type $Pbnm$ phase shows a maximized $T_C = 160$ K [36,37]. However, the introduction of Ba cation systematically reduces the octahedral distortion, leading to the cubic-type $Pm-3m$ phase forms at $x = 0.3-0.4$. In bulk series, the increased Ba concentration elongates the Ru-O bond, and saturates the T_C at 60 K for final member (BaRuO_3). The trend of T_C for the thin-film results presented here is in good agreement with the bulk series [36,37].

H. Discussion

We have systematically shown that epitaxial strain provides an effective platform to stabilize $\text{Sr}_{1-x}\text{Ba}_x\text{RuO}_3$ films. Investigation on a series of isovalent substitution revealed that this system is sensitive to structural tunings that can be used to manipulate electromagnetic properties. Low Ba concentration ($x \leq 0.2$) benefits an effective structural transition from orthorhombic ($a^- b^+ c^-$) to a purely tetragonal symmetry ($a^0 b^0 c^0$) by diminishing octahedral rotational distortion. Simultaneously, the initial Ba substitution ($x \leq 0.2$) to SrRuO_3 also enhances the ferromagnetism reflected by a slight increase of T_C which is maximized around $x = 0.2$ (see Table I). The physics associated with such a structure-property relationship can be understood based on the octahedron

rotational distortion-dependent FM model [39,70–72]. In this picture, the reduction of the orthorhombic distortion favors the enhancement of the electron itinerancy due to the increase of bandwidth and density of states at Fermi energy, which leads to enhancement of itinerant-type ferromagnetism as observed for initial Ba substitution ($x \leq 0.2$).

At the same time, under compressive strain constraint by SrTiO_3 , the in-plane lattice parameters of all films ($a_{pc} = b_{pc}$) are essentially the same as that of SrTiO_3 substrate. Consequently, the compressively strained SrRuO_3 shows a slight increase of the out-of-plane parameter (c_{pc}) that pushes toward a tetragonal-type pseudocubic unit cell ($c_{pc}/a_{pc} > 1$). Such pseudocubic-cell stretching ($c_{pc}/a_{pc} > 1$) noticeably amplifies with increasing Ba substitution [see Fig. 1(c), and Fig. S1], leading to an enhanced structural anisotropy. The enhanced tetragonality influences the $4d-t_{2g}$ orbital arrangement and occupancy. In bulk SrRuO_3 ($c_{pc}/a_{pc} = 1$), under an octahedral field (Δ_o), the Ru-4d state holds a low-spin configuration ($4d^4 : t_{2g}^{3\uparrow, 1\downarrow} e_g^0; S = 1$), whereas the t_{2g} (d_{xy}, d_{yz}, d_{xz}) states are nearly degenerate since the tetragonal-field splitting (Δ_T) is very small [Fig. 10(b)]. In the thin-film form such as that described in this work, the compressively strained SrRuO_3 or smaller Ba-concentration ($x \leq 0.2$) films under pseudocubic-cell elongation ($c_{pc}/a_{pc} > 1$) exhibit a splitting in d_{yz} and d_{xz} from the d_{xy} states due to a slight increase of Δ_T , whereas due to the antibonding nature, the d_{xy} are higher in energy than d_{yz} and d_{xz} [Fig. 10(b)]. The larger Ba substitution ($x \geq 0.5$) can further amplify the Δ_T splitting due to a large enhancement of pseudocubic-cell lengthening along out of plane ($c_{pc}/a_{pc} \gg 1$). As a result, a larger Δ_T split could partially transform the d_{xy} states to d_{yz}, d_{xz} and leads to even lower spin states that would result in the reduction of magnetic moment and FM order as seen for $x = 0.5$. Hence, the enhanced tetragonality with larger Ba substitution can diminish the ferromagnetism via

TABLE I. Pseudocubic lattice parameter, crystal symmetry, octahedra rotation pattern, Curie temperature (T_C), and magnetic moment of $\text{Sr}_{1-x}\text{Ba}_x\text{RuO}_3$ films.

x in $\text{Sr}_{1-x}\text{Ba}_x\text{RuO}_3$	Pseudocubic lattice parameter (\AA)	Crystal symmetry	Octahedra rotation pattern	T_C (K)	Magnetic moment (μ_B/Ru)
0	3.957	Orthorhombic	$a^- b^+ c^-$	145 ± 3	1.51
0.08	3.969	Tetragonal	$a^- b^+ c^- / a^+ b^- c$	149 ± 4	1.67
0.2	3.992	Tetragonal	$a^0 b^0 c^0$	146 ± 3	1.68
0.5	4.025	Tetragonal	$a^0 b^0 c^0$	100 ± 5	0.45
0.7	4.059	Tetragonal	$a^0 b^0 c^0$	80 ± 7	0.17

orbital redistribution. Such competing effects from structure to magnetism results in a nonmonotonic change of Curie temperature with Ba substitution. As the octahedral rotations disappear at $x \geq 0.2$, the effect of pseudocubic-cell stretching ($c_{pc}/a_{pc} \gg 1$) dominates with x and steadily suppresses the ferromagnetism of the system. In addition, the enhanced structural anisotropy also results in the enhanced perpendicular magnetic anisotropy with Ba substitution as observed from our experiments.

IV. CONCLUSION

In conclusion, we fabricated the $\text{Sr}_{1-x}\text{Ba}_x\text{RuO}_3$ ($0 \leq x \leq 0.7$) thin films. The strain-stabilized Ba substitution transmutes the lattice symmetry from bulklike orthorhombically distorted ($x = 0$) to tetragonal phase ($x = 0.2$) without RuO_6 rotations. The epitaxially stabilized tetragonal phase without RuO_6 rotations is ferromagnetically ($T_C \sim 145$ K) ordered with a strong perpendicular magnetic anisotropy, although increased Ba substitution ($x \geq 0.5$) significantly condenses the ferromagnetism via orbital reconstructions. The investigations provide an essential understanding of ruthenate ferromagnetism, indicating sensitivity to A site in determining the crystal structure as well as electromagnetic properties of ruthenates.

The data used in the study are available in the paper and Supplemental Material. The data that support the findings of this study are available from the corresponding author upon reasonable request.

ACKNOWLEDGMENTS

This work is primarily supported by the U.S. Department of Energy (DOE) under Grant No. DOE DE-SC0002136. The electron microscopy work done at Brookhaven National Laboratory (BNL) was sponsored by the U.S. DOE-BES, Materials Sciences and Engineering Division, under Contract No. DE-SC0012704. Use of the BNL Center for Functional Nanomaterials supported by the BES Office of User Science Facilities for TEM sample preparation is also acknowledged. Work at Oak Ridge National Laboratory was supported by the U.S. DOE, Office of Basic Energy Sciences (BES), Materials Sciences and Engineering Division. The work at Los Alamos National Laboratory was supported by the NNSA's Laboratory Directed Research and Development Program, and was performed, in part, at the CINT, an Office of Science User Facility operated for the U.S. Department of Energy Office of Science through the Los Alamos National Laboratory. Los Alamos National Laboratory is operated by Triad National Security, LLC, for the National Nuclear Security Administration of U.S. Department of Energy (Contract No. 89233218CNA000001).

Z.A., M.S., and J.Z. designed the research; Z.A. grew the samples and performed transport/magnetization measurements; Z.A. and M.S. performed the x-ray diffraction; Z.A. and R.N. prepared thin-film targets; Z.W. and Y.Z. carried out the STEM experiments; A.R.M. and T.Z.W. did half-angle x-ray diffraction; and Z.A. wrote the manuscript with input from all authors.

- [1] J. M. Rondinelli, S. J. May, and J. W. Freeland, Control of octahedral connectivity in perovskite oxide heterostructures: An emerging route to multifunctional materials discovery, *MRS Bull.* **37**, 261 (2012).
- [2] A. Bhattacharya and S. J. May, Magnetic oxide heterostructures, *Annu. Rev. Mater. Res.* **44**, 65 (2014).
- [3] H. Kobayashi, M. Nagata, R. Kanno, and Y. Kawamoto, Structural characterization of the orthorhombic perovskites: $[\text{ARuO}_3$ ($A = \text{Ca}, \text{Sr}, \text{La}, \text{Pr}$)], *Mater. Res. Bull.* **29**, 1271 (1994).
- [4] J.-S. Zhou, K. Matsubayashi, Y. Uwatoko, C.-Q. Jin, J.-G. Cheng, J. B. Goodenough, Q. Q. Liu, T. Katsura, A. Shatskiy, and E. Ito, Critical Behavior of the Ferromagnetic Perovskite BaRuO_3 , *Phys. Rev. Lett.* **101**, 077206 (2008).
- [5] G. Cao, S. McCall, M. Shepard, J. E. Crow, and R. P. Guertin, Thermal, magnetic, and transport properties of single-crystal $\text{Sr}_{1-x}\text{Ca}_x\text{RuO}_3$ ($0 < x < \sim 1.0$), *Phys. Rev. B* **56**, 321 (1997).
- [6] J. J. Hamlin, S. Deemyad, J. S. Schilling, M. K. Jacobsen, R. S. Kumar, A. L. Cornelius, G. Cao, and J. J. Neumeier, ac susceptibility studies of the weak itinerant ferromagnet SrRuO_3 under high pressure to 34 GPa, *Phys. Rev. B* **76**, 014432 (2007).
- [7] J. Pietosa, B. Dabrowski, A. Wisniewski, R. Puzniak, R. Kiyonagi, T. Maxwell, and J. D. Jorgensen, Pressure effects on magnetic and structural properties of pure and substituted SrRuO_3 , *Phys. Rev. B* **77**, 104410 (2008).
- [8] A. J. Williams, A. Gillies, J. P. Attfield, G. Heymann, H. Huppertz, M. J. Martínez-Lope, and J. A. Alonso, Charge

- transfer and antiferromagnetic insulator phase in $\text{SrRu}_{1-x}\text{Cr}_x\text{O}_3$: Solid solutions between two itinerant electron oxide, *Phys. Rev. B* **73**, 104409 (2006).
- [9] J. G. Cheng, J. S. Zhou, and J. B. Goodenough, Evolution of ferromagnetism in orthorhombic perovskites $\text{Sr}_{1-x}\text{Pb}_x\text{RuO}_3$, *Phys. Rev. B* **81**, 134412 (2010).
- [10] F. Fukunaga and N. Tsuda, On the magnetism and electronic conduction of itinerant magnetic system $\text{Ca}_{1-x}\text{Sr}_x\text{RuO}_3$, *J. Phys. Soc. Jpn.* **63**, 3798 (1994).
- [11] J. H. Haeni, P. Irvin, W. Chang, R. Uecker, P. Reiche, Y. L. Li, S. Choudhury, W. Tian, M. E. Hawley, B. Craigo, A. K. Tagantsev, X. Q. Pan, S. K. Streiffer, L. Q. Chen, S. W. Kirchoefer, J. Levy, and D. G. Schlom, Room-temperature ferroelectricity in strained SrTiO_3 , *Nature (London)* **430**, 758 (2004).
- [12] W. Lu, W. Song, P. Yang, J. Ding, G. M. Chow, and J. Chen, Strain engineering of octahedral rotations and physical properties of SrRuO_3 films, *Sci. Rep.* **5**, 10245 (2015).
- [13] D. Kan, R. Aso, H. Kurata, and Y. Shimakawa, Epitaxial strain effect in tetragonal SrRuO_3 thin films, *J. Appl. Phys.* **113**, 173912 (2013).
- [14] A. Vailionis, H. Boschker, W. Siemons, E. P. Houwman, D. H. A. Blank, G. Rijnders, and G. Koster, Misfit strain accommodation in epitaxial ABO_3 perovskites: Lattice rotations and lattice modulations, *Phys. Rev. B* **83**, 064101 (2011).
- [15] A. Vailionis, W. Siemons, and G. Koster, Room temperature epitaxial stabilization of a tetragonal phase in ARuO_3 ($A = \text{Ca}$ and Sr) thin films, *Appl. Phys. Lett.* **93**, 051909 (2008).
- [16] S. S. Hong, M. Gu, M. Verma, V. Harbola, B. Y. Wang, D. Lu, A. Vailionis, Y. Hikita, R. Pentcheva, J. M. Rondinelli, and H. Y. Hwang, Extreme tensile strain states in $\text{La}_{0.7}\text{Ca}_{0.3}\text{MnO}_3$ membranes, *Science* **368**, 71 (2020).
- [17] D. Kan, R. Aso, R. Sato, M. Haruta, H. Kurata, and Y. Shimakawa, Tuning magnetic anisotropy by interfacially engineering the oxygen coordination environment in a transition metal oxide, *Nat. Mater.* **15**, 432 (2016).
- [18] Z. Liao, M. Huijben, Z. Zhong, N. Gauquelin, S. Macke, R. J. Green, S. Van Aert, J. Verbeeck, G. Van Tendeloo, K. Held, G. A. Sawatzky, G. Koster, and G. Rijnders, Controlled lateral anisotropy in correlated manganite heterostructures by interface-engineered oxygen octahedral coupling, *Nat. Mater.* **15**, 425 (2016).
- [19] M. Meng, Z. Wang, A. Fathima, S. Ghosh, M. Saghayezhian, J. Taylor, R. Jin, Y. Zhu, S. T. Pantelides, J. Zhang, E. W. Plummer, and H. Guo, Interface-induced magnetic polar metal phase in complex oxides, *Nat. Commun.* **10**, 5248 (2019).
- [20] Z. Ali, Z. Wang, A. O'Hara, M. Saghayezhian, D. Shin, Y. Zhu, S. T. Pantelides, and J. Zhang, Origin of insulating and non-ferromagnetic SrRuO_3 monolayers, *Phys. Rev. B* **105**, 054429 (2022).
- [21] A. Herklotz, A. T. Wong, T. Meyer, M. D. Biegalski, H. N. Lee, and T. Z. Ward, Controlling octahedral rotations in a perovskite via strain doping, *Sci. Rep.* **6**, 26491 (2016).
- [22] E. Skoropata, A. R. Mazza, A. Herklotz, J. M. Ok, G. Eres, M. Brahlek, T. R. Charlton, H. N. Lee, and T. Z. Ward, Post-synthesis control of Berry phase driven magnetotransport in SrRuO_3 films, *Phys. Rev. B* **103**, 085121 (2021).
- [23] C. Wang, C. Chang, A. Herklotz, C. Chen, F. Ganss, U. Kentsch, D. Chen, X. Gao, Y. Zeng, O. Hellwig, M. Helm, S. Gemming, Y. Chu, and S. Zhou, Topological Hall effect in single thick SrRuO_3 layers induced by defect engineering, *Adv. Electron. Mater.* **6**, 2000184 (2020).
- [24] S. J. May, C. R. Smith, J.-W. Kim, E. Karapetrova, A. Bhattacharya, and P. J. Ryan, Control of octahedral rotations in $(\text{LaNiO}_3)^n/(\text{SrMnO}_3)^m$ superlattices, *Phys. Rev. B* **83**, 153411 (2011).
- [25] H. Guo, Z. Wang, S. Dong, S. Ghosh, M. Saghayezhian, L. Chen, Y. Weng, A. Herklotz, T. Z. Ward, R. Jin, S. T. Pantelides, Y. Zhu, J. Zhang, and E. W. Plummer, Interface-induced multiferroism by design in complex oxide superlattices, *Proc. Natl. Acad. Sci.* **114**, E5062 (2017).
- [26] C. Domínguez, A. B. Georgescu, B. Mundet, Y. Zhang, J. Fowler, A. Mercy, A. Waelchli, S. Catalano, D. T. L. Alexander, P. Ghosez, A. Georges, A. J. Millis, M. Gibert, and J. M. Triscone, Length scales of interfacial coupling between metal and insulator phases in oxides, *Nat. Mater.* **19**, 1182 (2020).
- [27] B. Chen, N. Gauquelin, R. J. Green, J. H. Lee, C. Piamonteze, M. Spreitzer, D. Jannis, J. Verbeeck, M. Bibes, M. Huijben, G. Rijnders, and G. Koster, Spatially controlled octahedral rotations and metal-insulator transitions in nickelate superlattices, *Nano Lett.* **21**, 1295 (2021).
- [28] K. Takiguchi, Y. K. Wakabayashi, H. Irie, Y. Krockenberger, T. Otsuka, H. Sawada, S. A. Nikolaev, H. Das, M. Tanaka, Y. Taniyasu, and H. Yamamoto, Quantum transport evidence of Weyl fermions in an epitaxial ferromagnetic oxide, *Nat. Commun.* **11**, 4969 (2020).
- [29] S. Lin, Q. Zhang, M. A. Roldan, S. Das, T. Charlton, M. R. Fitzsimmons, Q. Jin, S. Li, Z. Wu, S. Chen, H. Guo, X. Tong, M. He, C. Ge, C. Wang, L. Gu, K. Jin, and E.-J. Guo, Switching Magnetic Anisotropy of SrRuO_3 by Capping-Layer-Induced Octahedral Distortion, *Phys. Rev. Appl.* **13**, 034033 (2020).
- [30] D. Yi, J. Liu, S.-L. Hsu, L. Zhang, Y. Choi, J.-W. Kim, Z. Chen, J. D. Clarkson, C. R. Serrao, E. Arenholz, P. J. Ryan, H. Xu, R. J. Birgeneau, and R. Ramesh, Atomic-scale control of magnetic anisotropy via novel spin-orbit coupling effect in $\text{La}_{2/3}\text{Sr}_{1/3}\text{MnO}_3/\text{SrIrO}_3$ superlattices, *Proc. Natl. Acad. Sci.* **113**, 6397 (2016).
- [31] D. Yi, C. L. Flint, P. P. Balakrishnan, K. Mahalingam, B. Urwin, A. Vailionis, A. T. N'Diaye, P. Shafer, E. Arenholz, Y. Choi, K. H. Stone, J.-H. Chu, B. M. Howe, J. Liu, I. R. Fisher, and Y. Suzuki, Tuning Perpendicular Magnetic Anisotropy by Oxygen Octahedral Rotations in $(\text{La}_{1-x}\text{Sr}_x\text{MnO}_3)/(\text{SrIrO}_3)$ Superlattices, *Phys. Rev. Lett.* **119**, 077201 (2017).
- [32] B. Dieny and M. Chshiev, Perpendicular magnetic anisotropy at transition metal/oxide interfaces and applications, *Rev. Mod. Phys.* **89**, 025008 (2017).
- [33] Z. Ali, Controlling Electro-Magnetic Functionality of Ruthenates by Heterostructure Design, LSU Doctoral Dissertations (2022) 5972, https://digitalcommons.lsu.edu/gradschool_dissertations/5972.
- [34] H. Wang, G. Laskin, W. He, H. Boschker, M. Yi, J. Mannhart, and P. A. van Aken, Tunable magnetic anisotropy in patterned SrRuO_3 quantum structures: Competition between lattice anisotropy and oxygen octahedral rotation, *Adv. Funct. Mater.* **32**, 2108475 (2022).
- [35] L. T. Nguyen, M. Abeykoon, J. Tao, S. Lapidus, and R. J. Cava, Long-range and local crystal structures of the $\text{Sr}_{1-x}\text{Ca}_x\text{RuO}_3$ perovskites, *Phys. Rev. Mater.* **4**, 034407 (2020).

- [36] J. G. Cheng, J. S. Zhou, and J. B. Goodenough, Lattice effects on ferromagnetism in perovskite ruthenates, *Proc. Natl. Acad. Sci. USA* **110**, 13312 (2013).
- [37] C. Q. Jin, J. S. Zhou, J. B. Goodenough, Q. Q. Liu, J. G. Zhao, L. X. Yang, Y. Yu, R. C. Yu, T. Katsura, A. Shatskiy, and E. Ito, High-pressure synthesis of the cubic perovskite BaRuO₃ and evolution of ferromagnetism in ARuO₃ ($A = \text{Ca, Sr, Ba}$) ruthenates, *Proc. Natl. Acad. Sci.* **105**, 7115 (2008).
- [38] A. Callaghan, C. W. Moeller, and R. Ward, Magnetic interactions in ternary ruthenium oxides, *Inorg. Chem.* **5**, 1572 (1966).
- [39] I. I. Mazin and D. J. Singh, Electronic structure and magnetism in Ru-based perovskites, *Phys. Rev. B* **56**, 2556 (1997).
- [40] D. G. Schlom, L. Q. Chen, C. B. Eom, K. M. Rabe, S. K. Streiffer, and J. M. Triscone, Strain tuning of ferroelectric thin films, *Annu. Rev. Mater. Res.* **37**, 589 (2007).
- [41] J.-H. Lee, P. Murugavel, H. Ryu, D. Lee, J. Y. Jo, J. W. Kim, H. J. Kim, K. H. Kim, Y. Jo, M.-H. Jung, Y. H. Oh, Y.-W. Kim, J. G. Yoon, J.-S. Chung, and T. W. Noh, Epitaxial stabilization of a new multiferroic hexagonal phase of TbMnO₃ thin films, *Adv. Mater.* **18**, 3125 (2006).
- [42] P. A. Salvador, T.-D. Doan, B. Mercey, and B. Raveau, Stabilization of YMnO₃ in a perovskite structure as a thin film, *Chem. Mater.* **10**, 2592 (1998).
- [43] A. Kaul, O. Gorbenko, I. Graboy, M. Novojilov, A. Bosak, A. Kamenev, S. Antonov, I. Nikulin, A. Mikhaylov, and M. Kartavtzeva, Epitaxial stabilization in thin films of oxides, *MRS Proc.* **755**, 71 (2002).
- [44] J. P. Ruf, H. Paik, N. J. Schreiber, H. P. Nair, L. Miao, J. K. Kawasaki, J. N. Nelson, B. D. Faeth, Y. Lee, B. H. Goodge, B. Pamuk, C. J. Fennie, L. F. Kourkoutis, D. G. Schlom, and K. M. Shen, Strain-stabilized superconductivity, *Nat. Commun.* **12**, 59 (2021).
- [45] S. A. Lee, J. M. Ok, J. Lee, J. Hwang, S. Yoon, S. Park, S. Song, J. Bae, S. Park, H. N. Lee, and W. S. Choi, Epitaxial stabilization of metastable 3C BaRuO₃ thin film with ferromagnetic non-Fermi liquid phase, *Adv. Electron. Mater.* **7**, 2001111 (2021).
- [46] S. H. Chang, Y. J. Chang, S. Y. Jang, D. W. Jeong, C. U. Jung, Y.-J. Kim, J.-S. Chung, and T. W. Noh, Thickness-dependent structural phase transition of strained SrRuO₃ ultrathin films: The role of octahedral tilt, *Phys. Rev. B* **84**, 104101 (2011).
- [47] R. Gao, Y. Dong, H. Xu, H. Zhou, Y. Yuan, V. Gopalan, C. Gao, D. D. Fong, Z. Chen, Z. Luo, and L. W. Martin, Interfacial octahedral rotation mismatch control of the symmetry and properties of SrRuO₃, *ACS Appl. Mater. Interfaces* **8**, 14871 (2016).
- [48] P. M. Woodward, Octahedral tilting in Perovskites. I. Geometrical considerations, *Acta Crystallogr. Sect. B, Struct. Sci.* **53**, 32 (1997).
- [49] A. M. Glazer, The classification of tilted octahedra in perovskites, *Acta Crystallogr. Sect. B, Struct. Crystallogr. Cryst. Chem.* **28**, 3384 (1972).
- [50] W. Lu, P. Yang, W. D. Song, G. M. Chow, and J. S. Chen, Control of oxygen octahedral rotations and physical properties in SrRuO₃ films, *Phys. Rev. B* **88**, 214115 (2013).
- [51] M. Brahlek, A. K. Choquette, C. R. Smith, R. Engel Herbert, and S. J. May, Structural refinement of Pbnm-type perovskite films from analysis of half-order diffraction peaks, *J. Appl. Phys.* **121**, 045303 (2017).
- [52] S. J. May, J. W. Kim, J. M. Rondinelli, E. Karapetrova, N. A. Spaldin, A. Bhattacharya, and P. J. Ryan, Quantifying octahedral rotations in strained perovskite oxide films, *Phys. Rev. B* **82**, 014110 (2010).
- [53] Z. Ali, M. Saghayezhian, Z. Wang, A. O'Hara, D. Shin, W. Ge, Y. T. Chan, Y. Zhu, W. Wu, S. T. Pantelides, and J. Zhang, Emergent ferromagnetism and insulator-metal transition in δ -doped ultrathin ruthenates, *npj Quantum Mater.* **7**, 108 (2022).
- [54] P. Siwakoti, Z. Wang, M. Saghayezhian, D. Howe, Z. Ali, Y. Zhu, and J. Zhang, Abrupt orthorhombic relaxation in compressively strained ultra-thin SrRuO₃ films, *Phys. Rev. Mater.* **5**, 114409 (2021).
- [55] J. C. Jiang, W. Tian, X. Q. Pan, Q. Gan, and C. B. Eom, Domain structure of epitaxial SrRuO₃ thin films on miscut (001) SrTiO₃ substrates, *Appl. Phys. Lett.* **72**, 2963 (1998).
- [56] Q. Gan, R. A. Rao, and C. B. Eom, Control of the growth and domain structure of epitaxial SrRuO₃ thin films by vicinal (001) SrTiO₃ substrates, *Appl. Phys. Lett.* **70**, 1962 (1998).
- [57] G. Wang, Z. Wang, M. Meng, M. Saghayezhian, L. Chen, C. Chen, H. Guo, Y. Zhu, E. W. Plummer, and J. Zhang, Role of disorder and correlations in the metal-insulator transition in ultrathin SrVO₃ films, *Phys. Rev. B* **100**, 155114 (2019).
- [58] See Supplemental Material at <http://link.aps.org/supplemental/10.1103/PhysRevB.107.144405> for additional structural, magnetometry, and magnetotransport data.
- [59] P. B. Allen, H. Berger, O. Chauvet, L. Forro, T. Jarlborg, A. Junod, B. Revaz, and G. Santi, Transport properties, thermodynamic properties, and electronic structure of SrRuO₃, *Phys. Rev. B* **53**, 4393 (1996).
- [60] G. Koster, L. Klein, W. Siemons, G. Rijnders, J. S. Dodge, C.-B. Eom, D. H. A. A. Blank, and M. R. Beasley, Structure, physical properties, and applications of SrRuO₃, *Rev. Mod. Phys.* **84**, 253 (2012).
- [61] D. B. Kacedon, R. A. Rao, and C. B. Eom, Magnetoresistance of epitaxial thin films of ferromagnetic metallic oxide SrRuO₃ with different domain structures, *Appl. Phys. Lett.* **71**, 1724 (1997).
- [62] J. Q. Xiao, J. S. Jiang, and C. L. Chien, Giant Magnetoresistance in Nonmultilayer Magnetic Systems, *Phys. Rev. Lett.* **68**, 3749 (1992).
- [63] Z. Ali, D. Basaula, W. Zhou, J. Brock, M. Khan, and K. F. Eid, Controlling the charge transport mode in permalloy films using oblique angle deposition, *J. Magn. Magn. Mater.* **484**, 430 (2019).
- [64] J. Wu, J. W. Lynn, C. J. Glinka, J. Burley, H. Zheng, J. F. Mitchell, and C. Leighton, Intergranular Giant Magnetoresistance in a Spontaneously Phase Separated Perovskite Oxide, *Phys. Rev. Lett.* **94**, 037201 (2005).
- [65] H. Boschker, T. Harada, T. Asaba, R. Ashoori, A. V. Boris, H. Hilgenkamp, C. R. Hughes, M. E. Holtz, L. Li, D. A. Muller, H. Nair, P. Reith, X. Renshaw Wang, D. G. Schlom, A. Soukiassian, and J. Mannhart, Ferromagnetism and Conductivity in Atomically Thin SrRuO₃, *Phys. Rev. X* **9**, 011027 (2019).
- [66] Z. Ali, D. Basaula, K. F. Eid, and M. Khan, Anisotropic properties of oblique angle deposited permalloy thin films, *Thin Solid Films* **735**, 138899 (2021).
- [67] Z. Ali, *Growth, Transport, and Magnetic Properties of Oblique-Angle-Deposited Permalloy Thin Films* (Miami University, 2018).

- [68] D. Tian, Z. Liu, S. Shen, Z. Li, Y. Zhou, H. Liu, H. Chen, and P. Yu, Manipulating Berry curvature of SrRuO₃ thin films via epitaxial strain, *Proc. Natl. Acad. Sci.* **118**, 1 (2021).
- [69] M. Ziese and I. Vrejoiu, Anomalous and planar Hall effect of orthorhombic and tetragonal SrRuO₃ layers, *Phys. Rev. B* **84**, 104413 (2011).
- [70] K. Maiti, Role of covalency in the ground-state properties of perovskite ruthenates: A first-principles study using local spin density approximations, *Phys. Rev. B* **73**, 235110 (2006).
- [71] H. T. Dang, J. Mravlje, A. Georges, and A. J. Millis, Electronic correlations, magnetism, and Hund's rule coupling in the ruthenium perovskites SrRuO₃ and CaRuO₃, *Phys. Rev. B* **91**, 195149 (2015).
- [72] J. M. Rondinelli, N. M. Caffrey, S. Sanvito, and N. A. Spaldin, Electronic properties of bulk and thin film SrRuO₃: Search for the metal-insulator transition, *Phys. Rev. B* **78**, 155107 (2008).